



Degradation Analysis of Solid Oxide Fuel Cells with (La,Sr)(Co,Fe)O_{3-δ} Cathode/Gd₂O₃-CeO₂ Interlayer/Y₂O₃-ZrO₂ Electrolyte System: The Influences of Microstructural Change and Solid Solution Formation

Toshiaki Matsui,^{1b,*} Siqi Li, Yuki Inoue, Norifumi Yoshida, Hiroki Muroyama,^{*} and Koichi Eguchi^{*}

Department of Energy and Hydrocarbon Chemistry, Graduate School of Engineering, Kyoto University, Nishikyo-ku, Kyoto 615-8510, Japan

Solid oxide fuel cells with a configuration of (La,Sr)(Co,Fe)O_{3-δ} cathode/doped ceria interlayer/zirconia-based electrolyte have been extensively studied to elucidate the degradation mechanism. Various degradation factors were suggested, such as the formation of highly-resistive SrZrO₃ phase, and the reduction in active reaction sites because of the agglomeration of constituent materials. Among them, however, the influence of the ceria-zirconia solid solution formation at the doped ceria interlayer/zirconia-based electrolyte on the cell performance has not been elucidated sufficiently. In this study to achieve a comprehensive understanding of degradation phenomena at the cathode side, the chemical information of constituent materials, as well as the microstructural parameters, were analyzed for single cells before and after discharge operation. Especially, the ionic conductivity of solid solutions formed in the (La,Sr)(Co,Fe)O_{3-δ}/Gd₂O₃-CeO₂/Y₂O₃-ZrO₂ system was investigated in detail to clarify the ionic conductivity profile at the Gd₂O₃-CeO₂/Y₂O₃-ZrO₂ interface.

© The Author(s) 2019. Published by ECS. This is an open access article distributed under the terms of the Creative Commons Attribution Non-Commercial No Derivatives 4.0 License (CC BY-NC-ND, <http://creativecommons.org/licenses/by-nc-nd/4.0/>), which permits non-commercial reuse, distribution, and reproduction in any medium, provided the original work is not changed in any way and is properly cited. For permission for commercial reuse, please email: oa@electrochem.org. [DOI: 10.1149/2.0841904jes]



Manuscript submitted January 4, 2019; revised manuscript received February 19, 2019. Published March 2, 2019.

Solid oxide fuel cells (SOFCs) are promising power generation devices due to high energy conversion efficiency, high fuel flexibility, and low environmental load. Although several companies have commercialized SOFC systems,¹⁻³ the durability and reliability of SOFC cells/stacks have not been fully established. Further fundamental studies are required to clarify the degradation factors and mechanisms. In Japan, NEDO (New Energy and Industrial Technology Development Organization) managed a series of projects, which focused on the durability/reliability of SOFC stacks. Long-term performance tests by CRIEPI (Central Research Institute for Electric Power Industry) on six industrial stacks have revealed that the cathode degradation is dominant; in most stacks, the anode degradation rate was small.⁴

In real stacks, the mixed oxide ion-electron conductor of (La,Sr)(Co,Fe)O_{3-δ} (LSCF) is widely used as a cathode to achieve a good balance between the performance and the operating temperature. In this case, the cell configuration of LSCF cathode/doped ceria interlayer/zirconia-based electrolyte is generally adopted; a doped ceria interlayer serves as a diffusion barrier to prevent the solid state reaction between LSCF and zirconia-based electrolyte.⁵⁻¹⁴ Substantial efforts have been devoted to elucidate the degradation mechanism in this system, and multiple degradation factors were pointed out; e.g., *i*) the formation of highly-resistive SrZrO₃ (SZO) phase, *ii*) the agglomeration of LSCF and doped ceria phases, *iii*) the reduction in triple phase boundary length, and *iv*) the formation of ceria-zirconia solid solutions with low ionic conductivity. For the degradation factor *i*), the formation of SZO phase is inevitable when the porous interlayer is used.¹⁵⁻¹⁹ Furthermore, the cathodic polarization accelerates this chemical reaction.²⁰⁻²² Degradation factors *ii*) and *iii*) mainly reflect the reduction in electrochemically-active reaction sites.²² Although the last factor *iv*) has been recognized well,^{19,23-27} the influence of the ceria-zirconia solid solution formation on the cell performance has not been elucidated sufficiently.

Recently, we have reported the ionic conductivity of solid solutions formed in the Y₂O₃-ZrO₂ (YSZ) electrolyte layer for a single cell with a configuration of LSCF/Sm₂O₃-CeO₂/YSZ;²⁸ the composition of solid solutions was determined by STEM-EDS analysis. Samarium ion in the doped ceria interlayer migrated readily to the YSZ

electrolyte and formed the low-conductive solid solutions; their ionic conductivity was more than one order of magnitude lower than that of YSZ. It was concluded that the formation of Sm₂O₃-Y₂O₃-ZrO₂ solid solutions was mainly responsible for the lower conductivity. Furthermore, the doping effect of Sm³⁺ and Gd³⁺ on the conductivity of Y₂O₃-ZrO₂ phase was also studied. We found that the dopant species in the interlayer had a great impact on the ionic conductivity; the ionic conductivity of Sm₂O₃-Y₂O₃-ZrO₂ was significantly lower than that of Gd₂O₃-Y₂O₃-ZrO₂ even with the same dopant concentration.

In real stacks the interlayer of Gd₂O₃-CeO₂ is frequently applied, but the behavior of ionic conductivity in the vicinity of Gd₂O₃-CeO₂/YSZ interface, especially the doped ceria side, has not been elucidated. So, in this study, we mainly aimed to clarify the ionic conductivity profile at the Gd₂O₃-CeO₂/YSZ interface, based on the average structure. Furthermore, other degradation factors described above were also studied quantitatively to achieve a comprehensive understanding of degradation phenomena at the cathode side. Since the commercialized stacks are operated at < 800°C, accelerated tests were conducted at 1000°C to investigate the influence of the interdiffusion of constituent elements. After discharge operation of the cell for 400 h, the dissection analysis was conducted.

Experimental

The electrolyte-supported cell of Ni-YSZ|YSZ|GDC|LSCF was fabricated as follows. A disk of 8 mol% yttria-stabilized zirconia (abbreviated as YSZ, Tosoh, 24 mm in diameter, 500 μm in thickness) was used as an electrolyte. The Ni-YSZ cermet anode with a volume ratio of 60/40 was prepared from NiO (Wako Pure Chemical Industries) and YSZ powder (8 mol% Y₂O₃-ZrO₂, Tosoh). The mixture of NiO and YSZ was heat-treated at 1200°C for 5 h. The obtained powder was mixed with polyethylene glycol and 10 wt% carbon black to form a slurry. The resultant slurry of NiO-YSZ was screen-printed onto the electrolyte and subsequently fired at 1400 °C for 5 h in air. The slurry of Ce_{0.9}Gd_{0.1}O_{2-δ} (GDC, Shin-Etsu Chemical Co., Ltd.) was screen-printed on the other face of electrolyte, and then fired at 1250°C for 10 h in air. After that, La_{0.6}Sr_{0.4}Co_{0.2}Fe_{0.8}O₃ (LSCF, Kusaka rare metal products) was applied as a cathode; the slurry was screen-printed and subsequently fired at 1150°C for 5 h in air. The area of each electrode was 0.28 cm². The reference electrode of platinum wire was attached

*Electrochemical Society Member.

²E-mail: matsui@elech.kuic.kyoto-u.ac.jp

to surround the side edge of the YSZ disk and fixed by a platinum paste (Metalor Technologies (Japan) Corp.).

The single cell was sandwiched by alumina tubes with Pyrex glass seal. The anode was reduced under a hydrogen atmosphere at 1000°C prior to electrochemical measurements. The gases of 97% H₂–3% H₂O and O₂ were supplied to the anode and cathode, respectively, with a flow rate of 100 mL min⁻¹. Electrochemical measurements were conducted at 1000°C using the CellTest system (Solartron Analytical, potentiostat/galvanostat 1470E and frequency response analyzer 1455). For ac impedance measurements, the applied frequency was in the range of 0.1 Hz to 500 kHz with a voltage amplitude of 10 mV.

The microstructure of LSCF/GDC/YSZ system was analyzed quantitatively by using a focused ion beam–scanning electron microscope (FIB–SEM; NVision 40, Carl Zeiss–SIINT) equipped with an energy dispersive X-ray spectrometer (EDS; INCAxact, Oxford Instruments). The cells were infiltrated with the epoxy resin (Marumoto Struers KK) under vacuum conditions, and then cut and polished for the 3D reconstruction. The 2D cross-sectional SEM images (*x*–*y* plane) of the LSCF/GDC/YSZ system were collected along the *z*-direction with a spacing of about 30 nm by sequential milling-and-observation operation, as is the same manner in our previous reports.^{22,29–32} The 3D microstructure of LSCF/GDC/YSZ system was reconstructed in a computational field by aligning regularly spaced cross-sectional SEM images, and then the microstructural parameters were calculated.

Furthermore, solid solutions were synthesized from the corresponding metal nitrates via the coprecipitation method; Ce(NO₃)₃·6H₂O, Gd(NO₃)₃·6H₂O, ZrO(NO₃)₂·2H₂O, Sr(NO₃)₂ (Wako Pure Chemical Industries), and Y(NO₃)₃·6H₂O (Aldrich). Metal nitrates were dissolved in pure water, and then the pH of the solution was controlled to be 11 by adding aqueous ammonia (Wako Pure Chemical Industries). The resultant mixture was stirred overnight at 80°C, and subsequently dried at 120°C. The obtained coprecipitate was calcined at 700°C for 5 h in air. The resultant powders were cold-isostatically pressed into pellets at 300 MPa and sintered at 1600°C for 10 h in air; the atomic ratio of constituents in the sintered sample was identical to that of nominal composition. The relative density of sintered pellets was over 95%. The pellets were cut into the rectangular shape, ca. 3.5 mm × 3.5 mm × 8.0 mm. The ionic conductivity of resultant samples was measured at 600–1000°C in air by the dc four-probe method. The platinum paste and wire were applied as electrodes. Some pellets were grinded into powders, and their crystal structures were analyzed by X-ray diffraction (XRD, Rigaku Ultima IV X-ray diffractometer, Cu Kα). The working condition was 40 kV and 40 mA with a scanning rate of 5° min⁻¹. Raman spectroscopy was also performed for the phase identification by using LabRAM HR–800 (Horiba Jobin Yvon). Samples were irradiated with the Ar ion laser (Green line, 20 mW, 514.5 nm output).

Results and Discussion

Fig. 1 shows time courses of the potential and the ohmic resistance between the cathode and the reference electrode, and the polarization resistance of LSCF cathode during discharge (0.3 A cm⁻²) for 400 h at 1000°C. The ohmic and polarization resistances decreased significantly from the beginning of discharge up to ca. 20 h, and then gradually reduced up to 280 h. This performance improvement will be due to the current passage effect;³³ similar behavior was observed in our previous report with the LSCF/Sm₂O₃–CeO₂/YSZ system.²² Over 280 h of operation, resistances were changed into an increase, suggesting the progress of deterioration. Thus, the potential change in Fig. 1a can be explained by a series of changes in these resistive components. After this test, the post-dissection analysis was conducted.

The microstructural evolution upon discharge was quantitatively analyzed by FIB–SEM with focusing on the cathode side. The obtained parameters are summarized in Table I. The result for the single cell before discharge is also listed for comparison. After discharge operation, the length of active triple phase boundary (TPB) decreased drastically, which was in contact with open pore, GDC, and LSCF. The contact area between pore and LSCF, so-called as the double

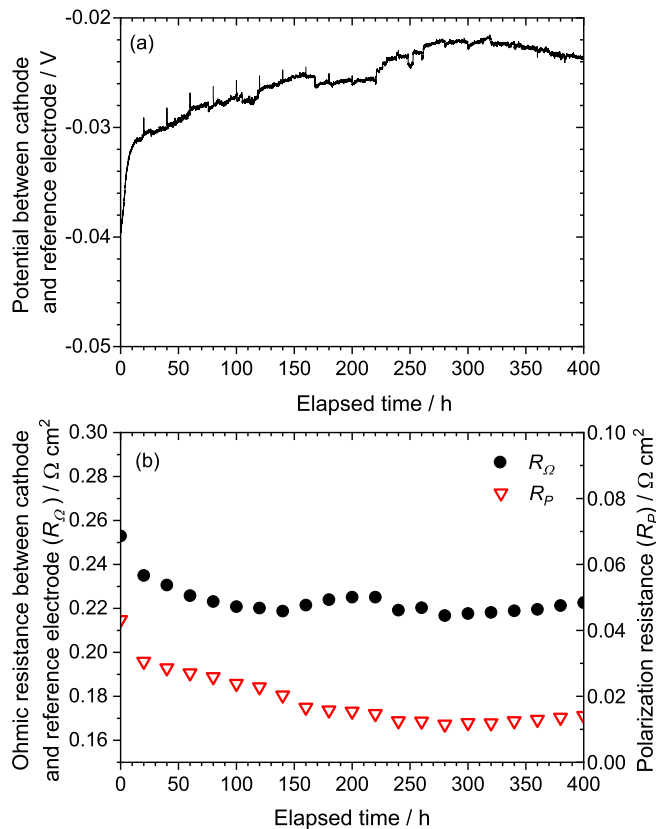


Figure 1. Time courses of (a) cathode-reference electrode potential and (b) ohmic (cathode-reference electrode) and polarization resistances of cathode for a single cell during discharge at 0.3 A cm⁻² for 400 h. Operating temperature: 1000°C; Cathode gas: O₂; Anode gas: 3% H₂O–97% H₂.

phase boundary area (abbreviated as DPB area), also reduced. Thus, the agglomeration of LSCF was the main reason for the reduction of active reaction parts. These factors will predominantly affect the polarization resistance. On the other hand, a reduction in the contact area between LSCF and GDC will mainly contribute to an increase

Table I. Microstructural parameters of reconstructed LSCF/GDC/YSZ systems before and after discharge at 0.3 A cm⁻² for 400 h.

		Operating time of the cell	
		0 h	400 h
Dimension (μm)	<i>x</i>	24.57	24.57
	<i>y</i>	12.36	12.36
	<i>z</i>	12.88	12.62
Contact area between LSCF and GDC/ <i>y</i> – <i>z</i> area (μm ² /μm ²)		0.51	0.33
Active TPB length/ <i>y</i> – <i>z</i> area (μm/μm ²)*		3.33	1.61
DPB area/LSCF volume (μm ² /μm ³)**		2.92	1.60
LSCF porosity (%)		43.6	33.2
SrZrO ₃ volume/ <i>y</i> – <i>z</i> area (μm ³ /μm ²)		0.0611	0.212
Co ₃ O ₄ and CoFe ₂ O ₄ volume/LSCF volume (μm ³ /μm ³)		0.0151	0.0279

*The length was calculated from the contact interface between open pore, GDC, and LSCF, and divided by the *y*–*z* area.

**The contact area between pore and LSCF was divided by the phase volume of LSCF.

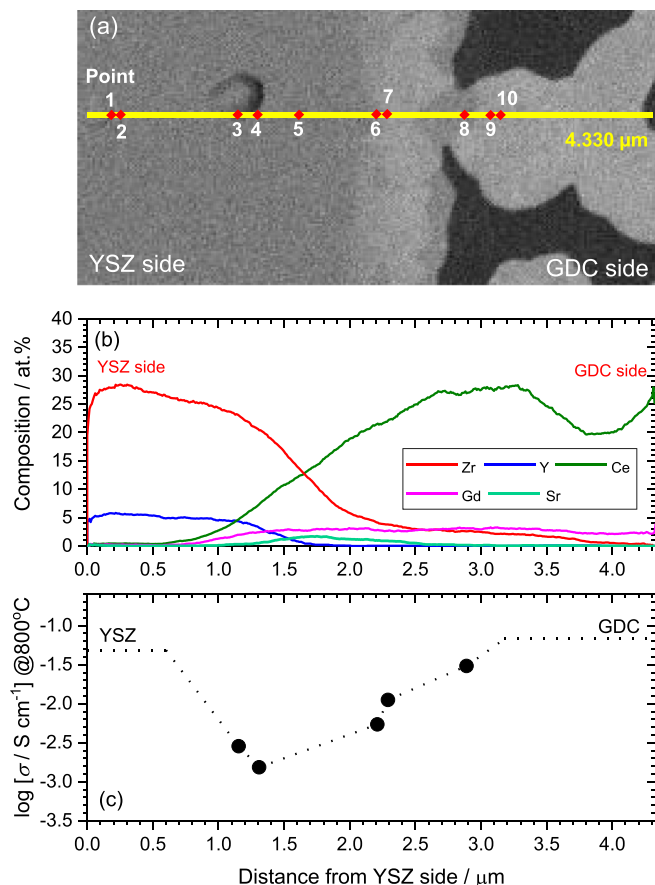


Figure 2. (a) The cross-sectional BSE image of GDC/YSZ interface before discharge, (b) the EDS line scan profile along the yellow line in (a), and (c) the ionic conductivity profile at 800°C predicted from Fig. 4.

in the ohmic resistance. Furthermore, the volume of highly-resistive SrZrO_3 phase in the vicinity of the GDC/YSZ interface was 3.5 times larger than that in the as-prepared cell, indicating that the current passage accelerated the SrZrO_3 formation. Note that the SrZrO_3 phase was located dispersedly, not formed a thin layer, as was reported in our previous report.²² The formation of by-products such as Co_3O_4 and CoFe_2O_4 phases was also confirmed by the EDS analysis, and its amount increased after discharge operation. Thus, we can guess that the segregation of A-site cation of Sr^{2+} in the LSCF lattice resulted in the formation of these oxides consisting of residual B-site elements.

In the next part, the influence of solid solutions formed at the porous GDC interlayer/YSZ electrolyte interface on the ionic conductivity was investigated precisely. Fig. 2a shows the cross-sectional back-scattered electron (BSE) image of the GDC/YSZ interface before discharge, which corresponds to the square part in Fig. S1(a) in the electronic supplementary information. Fig. 2b displays the line scan profile of constituent elements along the yellow line in Fig. 2a; this measurement was conducted by using SEM-EDS to obtain the composition information based on the average structure because the interfacial structure is complicated and its composition changes depending on analyzed points. The same series of BSE image and line scan profile after discharge is summarized in Figs. 3a and 3b. It is clear that the substantial interdiffusion of constituent elements occurred even during the cell fabrication process. Especially, the diffusion of gadolinium was prominent in the YSZ electrolyte side. Furthermore, the interdiffusion has progressed during the discharge operation. An increase in the amount of strontium was also observed, which agreed well with an increment in the volume of SrZrO_3 in the vicinity of the GDC/YSZ interface in Table I. Note that the diffusion of other cathode components, such as Co and Fe, was not detected. Subsequently, the

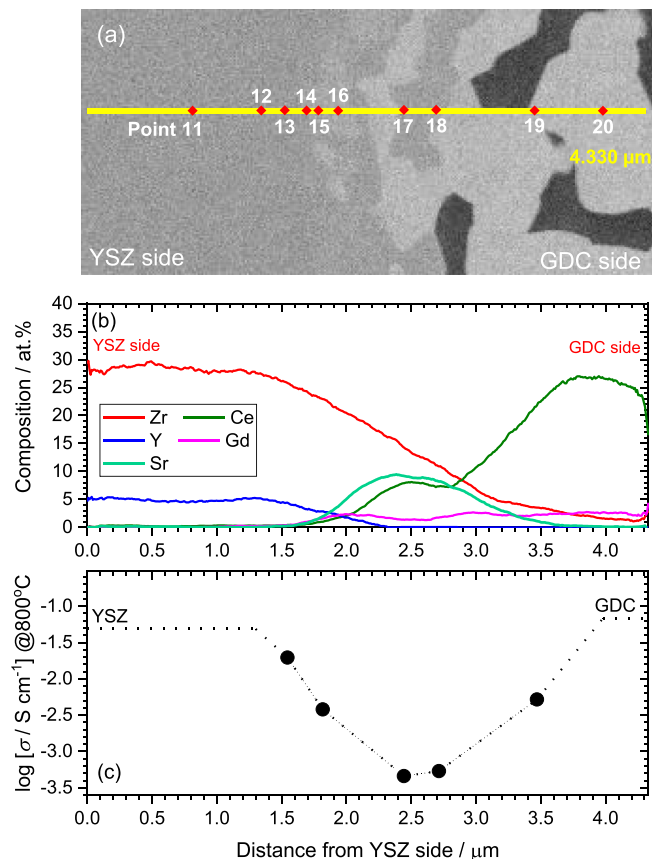


Figure 3. (a) The cross-sectional BSE images of GDC/YSZ interface after discharge for 400 h, (b) the EDS line scan profile along the yellow line in (a), and (c) the ionic conductivity profile at 800°C predicted from Fig. 5.

EDX data was analyzed in detail at points 1~20 in Figs. 2a and 3a. The atomic ratio of constituent elements at representative points was picked up and summarized in Table II with sample notations. Based on these results, solid solutions with corresponding compositions were synthesized and their crystalline structures were analyzed. The XRD patterns and Raman spectra of solid solutions are displayed in Figs. S2-S5 (electronic supplementary information), and the obtained phase information was summarized in Table II. For the as-prepared sample, the main phase of solid solutions was changed along the yellow line in Fig. 2a. At the YSZ side, solid solutions were the mixture of the cubic and tetragonal zirconia phases and $\text{Gd}_2(\text{Zr}_{1-x}\text{Ce}_x)_2\text{O}_7$ phase with the pyrochlore structure. The formation of SrZrO_3 phase was confirmed in the vicinity of GDC/YSZ interface, and then the main phase was changed to the fluorite-type ceria phase at the GDC side. This tendency was unchanged even after discharge operation.

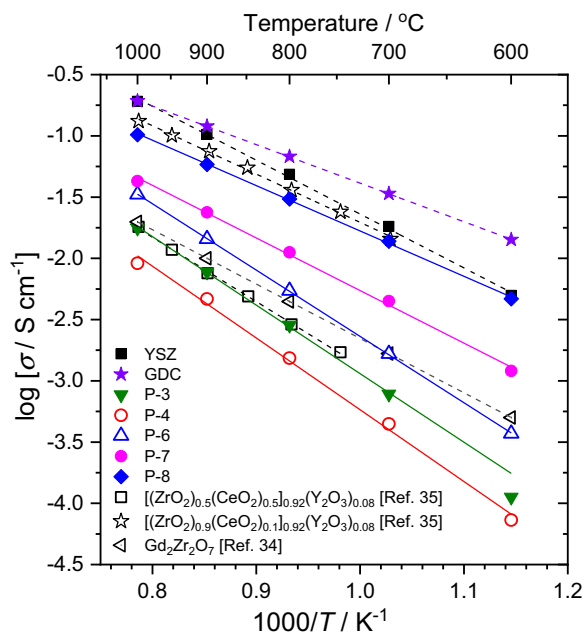
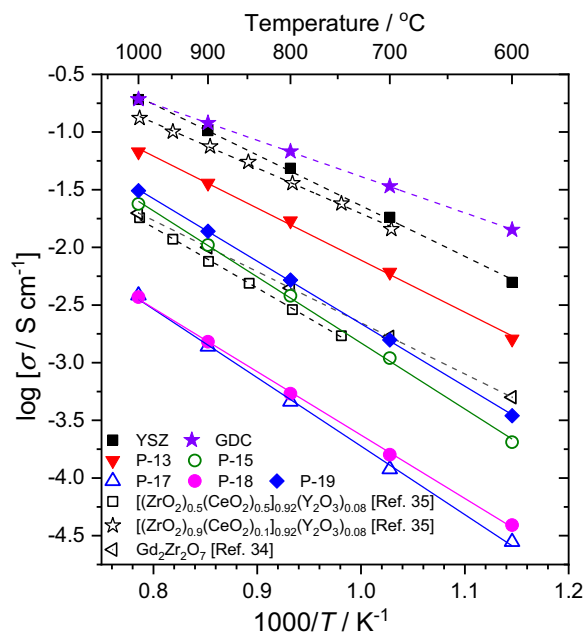
Figs. 4 and 5 show the temperature dependence of the ionic conductivity for solid solutions at 600–1000°C. The data for YSZ, GDC, $\text{Gd}_2\text{Zr}_2\text{O}_7$,³⁴ and $[(\text{ZrO}_2)_{1-x}(\text{CeO}_2)_x]_{0.92}(\text{Y}_2\text{O}_3)_{0.08}$ ($x = 0.1, 0.5$)³⁵ are also plotted for comparison. All solid solutions exhibited lower ionic conductivity as compared to YSZ and GDC. This result indicates that the elemental interdiffusion results in the formation of low conductivity region at the YSZ/GDC interface. Furthermore, the lowering extent of conductivity was significantly dependent on analyzed positions. For the as-prepared sample, the gradient of P-3 and P-4 was almost the same and was steeper than that of others. This can be explained by the difference in the main phase. The samples of P-3 and P-4 were the mixture of cubic-tetragonal zirconia phase and $\text{Gd}_2(\text{Zr}_{1-x}\text{Ce}_x)_2\text{O}_7$. The ionic conductivity of these samples was lower than that of ceria-zirconia solid solutions of $[(\text{ZrO}_2)_{1-x}(\text{CeO}_2)_x]_{0.92}(\text{Y}_2\text{O}_3)_{0.08}$ ($x = 0 \sim 0.5$). This result is the same as was observed in the LSCF/ Sm_2O_3 - CeO_2 /YSZ system.²⁸ Thus, the migration of gadolinium from the

Table II. Sample notation, atomic ratio of constituent elements, and phase information of solid solutions at representative points in Figs. 2a and 3a.

		Sample notation	Atomic ratio of constituent elements	Phase information
Before discharge	Point 3	P-3	Ce/Gd/Y/Zr = 1.0/1.0/1.7/7.2	Cubic-tetragonal zirconia phase, Gd ₂ (Zr _{1-x} Ce _x) ₂ O ₇
	Point 4	P-4	Ce/Gd/Y/Zr = 2.6/1.0/1.4/6.0	Cubic-tetragonal zirconia phase, Gd ₂ (Zr _{1-x} Ce _x) ₂ O ₇
	Point 6	P-6	Ce/Gd/Zr/Sr = 12.3/2.4/3.2/1.0	Fluorite-type ceria phase, SrZrO ₃
	Point 7	P-7	Ce/Gd/Zr/Sr = 10.1/1.7/2.1/1.0	Fluorite-type ceria phase, SrZrO ₃
	Point 8	P-8	Ce/Gd/Zr/Sr = 21.1/2.2/1.5/1.0	Fluorite-type ceria phase, SrZrO ₃
After discharge for 400 h	Point 13	P-13	Ce/Gd/Y/Zr = 1.0/1.0/2.9/18.6	Cubic-tetragonal zirconia phase, Gd ₂ (Zr _{1-x} Ce _x) ₂ O ₇
	Point 15	P-15	Ce/Gd/Y/Zr = 1.0/1.3/3.0/12.3	Cubic-tetragonal zirconia phase, Gd ₂ (Zr _{1-x} Ce _x) ₂ O ₇
	Point 17	P-17	Ce/Gd/Zr/Sr = 4.4/1.0/8.3/5.0	Fluorite-type ceria phase, SrZrO ₃
	Point 18	P-18	Ce/Gd/Zr/Sr = 4.9/1.0/5.8/5.2	Fluorite-type ceria phase, SrZrO ₃
	Point 19	P-19	Ce/Gd/Zr = 4.8/1.1/1.0	Fluorite-type ceria phase

interlayer side and the subsequent formation of Gd_2O_3 – Y_2O_3 – ZrO_2 solid solutions will be mainly responsible for the lower ionic conductivity. In Fig. 2a, the contrast of gray scale turned from dark gray to white gray in the vicinity of P-6 and P-7. This boundary can be roughly considered as the phase change region from the zirconia-based phase to the ceria-based phase; note that this part did not correspond exactly to the intersection point between the zirconium and cerium lines in Fig. 2b. In fact, the main phase of P-6, P-7, and P-8 was the fluorite-type ceria and a little amount of SrZrO_3 was contained. Considering that these solid solutions exhibited higher conductivity than SrZrO_3 itself, the impact of insulating SrZrO_3 phase on the total conductivity is not significant; the ionic conductivity of SrZrO_3 is ca. 10^{-5} – 10^{-4} S cm^{-1} at 1000°C .³⁶ On the other hand, after 400 h of discharge, the distribution of ionic conductivity was different from that in the as-prepared sample. The samples of P-13 and P-15 exhibited higher conductivity than P-3 and P-4 while these materials had the same main phases; the ionic conductivity of P-13 and P-15 was located between $[(\text{ZrO}_2)_{1-x}(\text{CeO}_2)_x]_{0.92}(\text{Y}_2\text{O}_3)_{0.08}$ ($x = 0.1 \sim 0.5$). This will be due to the lower gadolinium ratio in these solid solutions. Note that the significant reduction in the ionic conductivity was confirmed for P-17 and P-18; their conductivity was almost two orders of magnitude lower than that of GDC at 1000°C . Judging from the

structural analysis, it can be expected that a certain amount of insulating SrZrO_3 phase was formed. This will result in the significant reduction in the ionic conductivity. This expectation coincides to the fact that as can be seen in Fig. 3a, P-17 and P-18 were located on a dark gray region, which was a SrZrO_3 -concentrated region. If such a SrZrO_3 -enriched part formed a continuous thin layer, the ionic conduction will be inhibited considerably. J. Szász et al. reported that the firing temperature of GDC interlayer affects the formation process of SrZrO_3 -concentrated region.¹⁹ Whereas in this study the formation of continuous thin layer was not observed, we need to pay attention to this phenomenon during the long-term operation because of the acceleration of strontium migration under a discharge condition. Although P-19 consisted of the fluorite-type ceria phase with an atomic ratio of $\text{Ce/Gd/Zr} = 4.8/1.1/1.0$, its conductivity was about one order of magnitude lower than that of GDC. Since the Ce/Gd ratio in P-19 was close to that in $\text{Ce}_{0.8}\text{Gd}_{0.2}\text{O}_{2-\delta}$, the additive effect of zirconium to $(\text{Ce,Gd})\text{O}_2$ was studied. Since P-19 can be roughly considered as the $\text{Ce}_{0.8}\text{Gd}_{0.2}\text{O}_{2-\delta}$ -based solid solution dissolved with 14% of zirconium, its conductivity was compared with the pristine $\text{Ce}_{0.8}\text{Gd}_{0.2}\text{O}_{2-\delta}$ ³⁷ and the $\text{Ce}_{0.8}\text{Gd}_{0.2}\text{O}_{2-\delta}$ -based solid solution dissolved with 10% of zirconium (see Fig. 6). It is apparent that the addition of zirconium led to the drastic reduction in the ionic conductivity. Furthermore, the ionic

**Figure 4.** Temperature dependence of the ionic conductivity of solid solutions formed in the vicinity of GDC/YSZ interface in Fig. 2a. For comparison, the data for YSZ, GDC, $\text{Gd}_2\text{Zr}_2\text{O}_7$,³⁴ and $[(\text{ZrO}_2)_{1-x}(\text{CeO}_2)_x]_{0.92}(\text{Y}_2\text{O}_3)_{0.08}$ ($x = 0.1, 0.5$)³⁵ are also plotted.**Figure 5.** Temperature dependence of the ionic conductivity of solid solutions formed in the vicinity of GDC/YSZ interface in Fig. 3a. For comparison, the data for YSZ, GDC, $\text{Gd}_2\text{Zr}_2\text{O}_7$,³⁴ and $[(\text{ZrO}_2)_{1-x}(\text{CeO}_2)_x]_{0.92}(\text{Y}_2\text{O}_3)_{0.08}$ ($x = 0.1, 0.5$)³⁵ are also plotted.

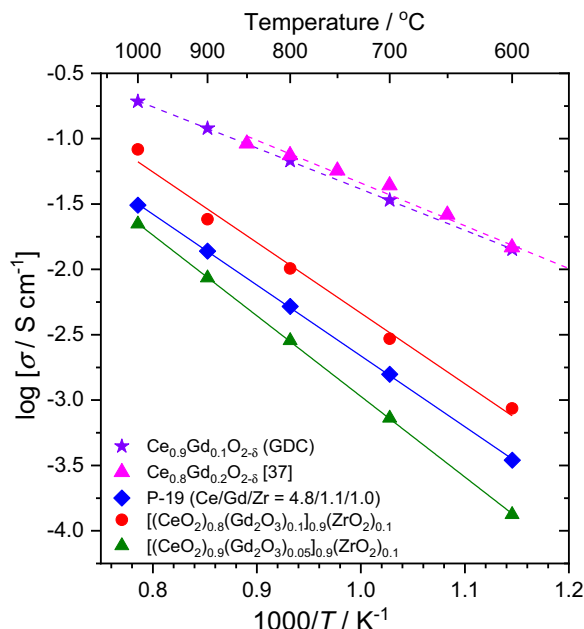


Figure 6. Temperature dependence of the ionic conductivity of P-19, GDC, $\text{Ce}_{0.8}\text{Gd}_{0.2}\text{O}_{2-x}$,³⁷ $[(\text{CeO}_2)_{0.8}(\text{Gd}_2\text{O}_3)_{0.1}]_{0.9}(\text{ZrO}_2)_{0.1}$, and $[(\text{CeO}_2)_{0.9}(\text{Gd}_2\text{O}_3)_{0.05}]_{0.9}(\text{ZrO}_2)_{0.1}$.

conductivity decreased with an increase in a zirconium content. When these temperature dependences of ionic conductivity were examined from the viewpoint of a gadolinium content in the sample, a high content of gadolinium mitigated the reduction in the ionic conductivity; the $\text{Ce}_{0.9}\text{Gd}_{0.1}\text{O}_{2-x}$ -based solid solution dissolved with 10% of zirconium exhibited lower conductivity, compared with the $\text{Ce}_{0.8}\text{Gd}_{0.2}\text{O}_{2-x}$ -based solid solution dissolved with 10% of zirconium though the ionic conductivity of pristine $\text{Ce}_{0.9}\text{Gd}_{0.1}\text{O}_{2-x}$ and $\text{Ce}_{0.8}\text{Gd}_{0.2}\text{O}_{2-x}$ was almost comparable with each other. Consequently, the zirconium dissolution to the ceria-based oxide is responsible for the lower conductivity of P-19.

Figs. 2c and 3c show the ionic conductivity profiles at 800°C along the yellow line in Figs. 2a and 3a, respectively; the ionic conductivity at each point was extracted from Figs. 4 and 5. In both cases, a low conductive region was formed at the YSZ/GDC interface with a thickness of ca. 2~3 μm . This tendency is similar to that observed for ceria-zirconia solid solutions; the ionic conductivity shows the downward convex curve depending on the composition at fixed temperatures, as is reported for $(\text{Ce}_x\text{Zr}_{1-x})_{0.8}\text{Y}_{0.2}\text{O}_{1.9-x}$ ($0 < x < 1$).³³ Note that a low conductive region was formed even soon after the cell fabrication process. However, the shape of downward convex curve was somewhat different depending on a current passage condition; a downward convex curve was expanded in the depth direction after discharge operation because of a significant reduction in the ionic conductivity of solid solutions. This will be induced by the continuous interdiffusion of elements during the discharge operation. Therefore, this will become a potential degradation factor upon prolonged operation, leading to an increase in the ohmic loss.

Conclusions

In this study, degradation factors at the cathode side in the LSCF/GDC/YSZ system were comprehensively studied. As is reported by many researchers, the significant microstructural change upon discharge was observed; the formation of highly-resistive SrZrO_3 phase, and the reduction in active reaction sites because of the agglomeration and elemental diffusion of constituent materials. Furthermore, we found that the formation of solid solutions at the GDC/YSZ interface has a great potential to degrade the cell performance upon

prolonged operation. At the YSZ side, the migration of gadolinium from the GDC interlayer side and the subsequent formation of Gd_2O_3 - Y_2O_3 - ZrO_2 solid solutions resulted in the reduction in the ionic conductivity. On the other hand, at the GDC side, the zirconium dissolution to the ceria-based oxide was responsible for the lower conductivity. As a result, the ionic conductivity profile at the GDC/YSZ interface has revealed that a low conductive region was formed with a thickness of ca. 2~3 μm even soon after the cell fabrication process. Furthermore, this specific region was expanded after discharge operation because of the continuous interdiffusion of elements, accompanied by a significant reduction in the conductivity. Thus, a multilateral analysis is indispensable to understand and predict the degradation phenomena at the cathode side upon long-term discharge operation.

Acknowledgment

This work was supported by the New Energy and Industrial Technology Development Organization (NEDO), Japan (Development of System and Elemental Technology on Solid Oxide Fuel Cell Project).

ORCID

Toshiaki Matsui  <https://orcid.org/0000-0003-1584-0304>

References

- K. Horiuchi, *ECS Transactions*, **57**, 3 (2013).
- H. Yokokawa, *ECS Transactions*, **57**, 299 (2013).
- M. Suzuki, Y. Takuwa, S. Inoue, and K. Higaki, *ECS Transactions*, **57**, 309 (2013).
- H. Yokokawa, Y. Hori, T. Shigehisa, M. Suzuki, S. Inoue, T. Suto, K. Tomida, M. Shimazu, A. Kawakami, H. Sumi, M. Ohmori, N. Mori, T. Iha, K. Yamaji, H. Kishimoto, K. Develos-Bagarinao, K. Sasaki, S. Taniguchi, T. Kawada, M. Muramatsu, K. Terada, K. Eguchi, H. Iwai, T. Matsui, M. Kishimoto, N. Shikazono, T. Yamamoto, Y. Mugikura, M. Yoshikawa, K. Yasumoto, K. Asano, Y. Matsuzaki, S. Amaha, and T. Somekawa, *Fuel Cells*, **17**, 473 (2017).
- H. Uchida, S. Arisaka, and M. Watanabe, *Electrochem. Solid-State Lett.*, **2**, 428 (1999).
- H. Uchida, S. Arisaka, and M. Watanabe, *Solid State Ionics*, **135**, 347 (2000).
- S. Uhlenbruck, T. Moskalowicz, N. Jordan, H. J. Penkalla, and H. P. Buchkremer, *Solid State Ionics*, **180**, 418 (2009).
- A. Mai, V. A. C. Haanappel, S. Uhlenbruck, F. Tietz, and D. Stöver, *Solid State Ionics*, **176**, 1341 (2005).
- A. Mai, M. Becker, W. Assenmacher, F. Tietz, D. Hathiraman, E. Ivers-Tiffée, D. Stöver, and W. Mader, *Solid State Ionics*, **177**, 1965 (2006).
- N. Sakai, H. Kishimoto, K. Yamaji, T. Horita, M. E. Brito, and H. Yokokawa, *J. Electrochem. Soc.*, **154**, B1331 (2007).
- W. H. Kim, H. S. Song, J. Moon, and H. W. Lee, *Solid State Ionics*, **177**, 3211 (2006).
- M. Izuki, M. E. Brito, K. Yamaji, H. Kishimoto, D. H. Cho, T. Shimonosono, T. Horita, and H. Yokokawa, *J. Power Sources*, **196**, 7232 (2011).
- J. Szász, F. Wankmüller, V. Wilde, H. Störmer, D. Gerthsen, N. H. Menzler, and E. Ivers-Tiffée, *ECS Transactions*, **66**, 79 (2015).
- V. Wilde, H. Störmer, J. Szász, F. Wankmüller, E. Ivers-Tiffée, and D. Gerthsen, *ECS Transactions*, **66**, 103 (2015).
- R. Knibbe, J. Hjelm, M. Menon, N. Pryds, M. Søgaard, H. J. Wang, and K. Neufeld, *J. Am. Ceram. Soc.*, **93**, 2877 (2010).
- N. Jordan, W. Assenmacher, S. Uhlenbruck, V. A. C. Haanappel, H. P. Buchkremer, D. Stöver, and W. Mader, *Solid State Ionics*, **179**, 919 (2008).
- J. Hjelm, M. Søgaard, R. Knibbe, A. Hagen, and M. Mogensen, *ECS Transactions*, **13**, 285 (2008).
- F. Wankmüller, J. Szász, J. Joos, V. Wilde, H. Störmer, D. Gerthsen, and E. Ivers-Tiffée, *J. Power Sources*, **360**, 399 (2017).
- J. Szász, F. Wankmüller, V. Wilde, H. Störmer, D. Gerthsen, N. H. Menzler, and E. Ivers-Tiffée, *J. Electrochem. Soc.*, **165**, F898 (2018).
- F. Wang, M. E. Brito, K. Yamaji, D.-H. Cho, M. Nishi, H. Kishimoto, T. Horita, and H. Yokokawa, *Solid State Ionics*, **262**, 454 (2014).
- H. Yokokawa, N. Sakai, T. Horita, K. Yamaji, M. E. Brito, and H. Kishimoto, *J. Alloy. Compd.*, **452**, 41 (2008).
- T. Matsui, M. Komoto, H. Muroyama, K. Kishida, H. Inui, and K. Eguchi, *J. Power Sources*, **312**, 80 (2016).
- A. Tsoga, A. Gupta, A. Naoumidis, and P. Nikolopoulos, *Acta Materialia*, **48**, 4709 (2000).
- D. Zhou, B. Scarfino, and H. U. Anderson, *Solid State Ionics*, **175**, 19 (2004).
- N. M. Sammes, G. A. Tompsett, and Z. H. Cai, *Solid State Ionics*, **121**, 121 (1999).
- H. Mitsuyasu, Y. Nonaka, K. Eguchi, and H. Arai, *J. Solid State Chem.*, **129**, 74 (1997).
- H. Mitsuyasu, Y. Nonaka, and K. Eguchi, *Solid State Ionics*, **113-115**, 279 (1998).
- T. Matsui, S. Li, H. Muroyama, K. Kishida, H. Inui, and K. Eguchi, *Solid State Ionics*, **300**, 135 (2017).

29. H. Iwai, N. Shikazono, T. Matsui, H. Teshima, M. Kishimoto, R. Kishida, D. Hayashi, K. Matsuzaki, D. Kanno, M. Saito, H. Muroyama, K. Eguchi, N. Kasagi, and H. Yoshida, *J. Power Sources*, **195**, 955 (2010).
30. T. Matsui, Y. Mikami, H. Muroyama, and K. Eguchi, *J. Electrochem. Soc.*, **157**, B1790 (2010).
31. T. Matsui, Y. Mikami, H. Muroyama, and K. Eguchi, *J. Power Sources*, **242**, 790 (2013).
32. T. Matsui, M. Komoto, H. Muroyama, and K. Eguchi, *Fuel Cells*, **14**, 1022 (2014).
33. J.-P. Eufinger, M. Daniels, K. Schmale, S. Berendts, G. Ulbrich, M. Lerch, H.-D. Wiemhöfer, and J. Janek, *Phys. Chem. Chem. Phys.*, **16**, 25583 (2014).
34. H. Yamamura, H. Nishino, K. Kakinuma, and K. Nomura, *Solid State Ionics*, **158**, 359 (2003).
35. C. H. Lee and G. M. Choi, *Solid State Ionics*, **135**, 653 (2000).
36. F. W. Poulsen and N. van der Puil, *Solid State Ionics*, **53–56**, 777 (1992).
37. S. Zha, C. Xia, and G. Meng, *J. Power Sources*, **115**, 44 (2003).